ELECTRON MICROSCOPY

Single-atom vibrational spectroscopy in the scanning transmission electron microscope

F. S. Hage[1], G. Radtke[2]*, D. M. Kepaptsoglou[1,3], M. Lazzeri[2], Q. M. Ramasse[1,4]*

Single-atom impurities and other atomic-scale defects can notably alter the local vibrational responses of solids and, ultimately, their macroscopic properties. Using high-resolution electron energy-loss spectroscopy in the electron microscope, we show that a single substitutional silicon impurity in graphene induces a characteristic, localized modification of the vibrational response. Extensive ab initio calculations reveal that the measured spectroscopic signature arises from defect-induced pseudo-localized phonon modes—that is, resonant states resulting from the hybridization of the defect modes and the bulk continuum—with energies that can be directly matched to the experiments. This finding realizes the promise of vibrational spectroscopy in the electron microscope with single-atom sensitivity and has broad implications across the fields of physics, chemistry, and materials science.

Changes in the normal mode frequencies of dynamical systems that arise from the presence of impurities have been studied since the 19th century, which has resulted in the set of classical theorems now referred to as the Rayleigh theorems (*1*, *2*). However, the modern theory of defect modes in crystals was established in the 1940s with the pioneering work of Lifschitz (*3*). Many studies followed, mainly based on optical spectroscopies (*4*), which identified two types of nontrivial defect-induced modes known as localized and resonant modes. Resonant modes are also called quasi- or pseudo-localized modes because, despite being spatially extended, they involve a large-amplitude vibration of the impurity itself. Defect modes can control materials' properties such as electric and heat transport or, more generally, processes that are affected by the scattering of electrons or phonons. This can be exploited, for example, to suppress heat propagation in thermoelectrics using rattler modes (*5*), to tune the superconductivity in two-dimensional films (*6*), or to affect the optoelectronic properties of conducting polymers (*7*). Although the existence of an atomically localized spectroscopic signature of single-atom defects has long been discussed (*8*), conventional vibrational spectroscopies typically average information over much larger length scales.

Vibrational electron energy-loss spectroscopy (EELS) in the scanning transmission electron microscope (STEM) has recently emerged as a powerful means of probing the vibrational response of materials at a spatial resolution that is superior to that of other experimental techniques (*9*, *10*). Tip-enhanced Raman spectroscopy (TERS) (*11*) and inelastic electron tunneling spectroscopy (IETS) (*12*, *13*) provide high spatial and energy resolution alternatives, but they are strictly limited to surface experiments and, therefore, present challenges for a range of applications. Vibrational STEM-EELS, on the other hand, takes advantage of versatile probe-forming optics to offer ground-breaking capabilities: nanometer-scale thermometry (*14*), mapping of bulk and surface-phonon-polariton modes (*15*), establishing phonon dispersion diagrams from nano-objects (*16*), and site-specific isotopic labeling in molecular aggregates (*17*). These reports highlight the complementarity of STEM-EELS with conventional vibrational spectroscopies whose energy resolutions remain unmatched. However, the ultimate promise of vibrational STEM-EELS is the ability to reach the single-atom or molecular level, in the same way that modern microscopes have enabled electronic structure analysis (*18*), plasmonic (*19*) and UV-optical response fingerprinting (*20*), and energy-dispersive x-ray spectroscopy (*21*) from single atoms. Atomically resolved phonon maps of bulk systems are preliminary steps in this direction (*22*).

In this work, we use STEM-EELS to measure the localized vibrational signature of a single trivalent substitutional Si atom in single-layer graphene (Si@Gr). From ab initio simulations, we attribute the measured atomic-scale spectroscopic response to scattering by pseudo-localized vibrational modes arising from a resonance between the Si impurity–specific modes and the bulk continuum.

Figure 1A illustrates how electron beam deflectors are adjusted to displace the EEL spectrometer entrance aperture by 69 mrad (or an 8.87-Å^{-1} momentum transfer) with respect to the bright field (BF) disc so that these no longer overlap. Further details of the experimental geometry are provided in the supplementary materials (fig. S1). Compared with a conventional on-axis geometry, where the EELS aperture is centered on the BF disc, this off-axis or dark-field EELS geometry markedly suppresses the relative contributions of electrons having undergone elastic and delocalized phonon scattering, favoring instead highly localized impact phonon scattering (*23*). This approach makes it possible to record atomic-resolution phonon scattering maps of nanometer-thick flakes of hexagonal boron nitride (*22*) or of single-layer graphene (fig. S2), where the off-axis geometry is key because the on-axis EELS phonon response of graphene is vanishingly small (*24*). Note that the large beam convergence that is necessary for an atomic-sized probe results in spectral integration over a range of momentum transfer in the sample plane. To achieve a signal-to-noise ratio sufficient for resolving the phonon loss spectrum fine structure, the electron beam is scanned repeatedly over a small window, tightly defined around the impurity of interest, while the spectrum intensity is accumulated (*25*).

Figure 1B shows a dark-field EEL spectrum from a single Si atom impurity in graphene (labeled Si) alongside that acquired from a comparably sized region of pristine graphene (labeled C), located only a few atoms away from the Si impurity. The relative positions of the two scanned regions are indicated by red (Si) and blue (C) boxes on the high-angle annular dark-field (HAADF) image in Fig. 1C. A close-up of the probed Si atom (Fig. 1D) and the corresponding fine structure of the Si $L_{2,3}$ ionization edge (fig. S3C) confirm that the brighter-contrast Si atom is trivalently substituted into the graphene lattice. Asymmetric annular dark-field (aADF, thus denoted because of the off-axis geometry) movies were recorded during spectrum acquisition to monitor possible beam-induced structure modifications, while ensuring that the probed atom remained centered within the scanned region. Averaged aADF movies are shown as insets in Fig. 1B, with individual frames shown in the supplementary materials.

The Si and C spectra in Fig. 1B are normalized to the maximum of their respective zero-loss peaks (ZLPs). As a result, the tails of the ZLPs closely overlap immediately before the first observable loss features, which allows for a straightforward visual comparison of relative changes in energy loss caused by inelastic scattering by phonons. Any change in spectrum intensity above the coinciding ZLP tails should be representative of differences in relative phonon scattering probability. The fine structure in the phonon energy range of the two recorded spectra is strikingly different. Although the C spectrum is consistent with that of nondoped bulk graphene (*24*), the Si spectrum comprises phonon loss features at different energies.

[1]SuperSTEM Laboratory, SciTech Daresbury Campus, Daresbury WA4 4AD, UK. [2]Sorbonne Université, Muséum National d'Histoire Naturelle, UMR CNRS 7590, Institut de Minéralogie, de Physique des Matériaux et de Cosmochimie, 75005 Paris, France. [3]York Nanocentre and Department of Physics, University of York, Heslington, York YO10 5DD, UK. [4]School of Chemical and Process Engineering and School of Physics and Astronomy, University of Leeds, Leeds LS2 9JT, UK.
*Corresponding author. Email: qmramasse@superstem.org (Q.M.R.); guillaume.radtke@sorbonne-universite.fr (G.R.)

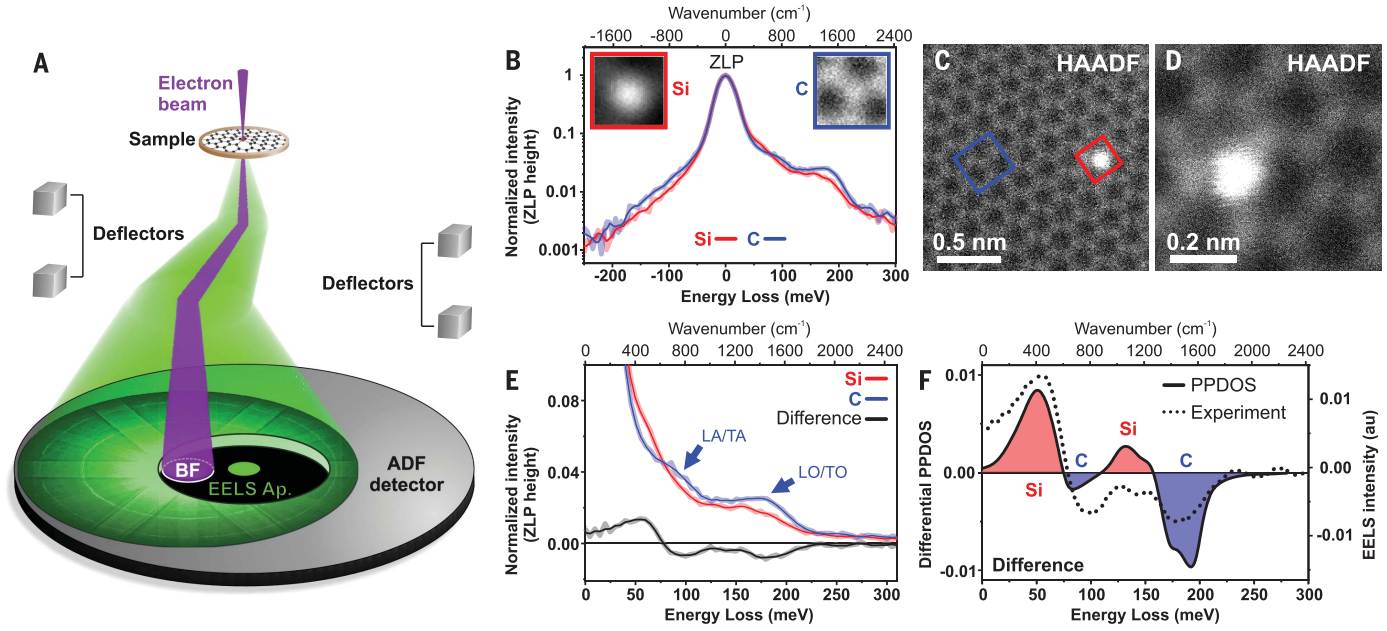

Fig. 1. Experimental geometry and vibrational STEM-EEL spectrum of a Si impurity in graphene. (**A**) Beam deflectors shift the BF disc away from the EEL spectrometer entrance aperture (Ap.) in the diffraction plane. (**B**) Normalized vibrational EEL spectra of a substitutional Si impurity and of defect-free graphene. Insets show aADF images of the repeatedly scanned sample regions. Smoothed spectra (thin lines) are superimposed on the raw data (shading around the lines). (**C**) HAADF overview of the experimental region. Red and blue boxes indicate the positions of the sub-scan regions from which the Si and C spectra, respectively, were acquired. (**D**) HAADF close-up of the (bright) trivalent Si impurity. (**E**) Detail of the normalized Si and C EEL spectra shown in (B) and the difference spectrum. L, longitudinal; T, transverse; A, acoustic; O, optical. (**F**) Comparison of the calculated differential PPDOS (broadened to match the experimental resolution) and the experimental difference spectrum. The blue and red shaded areas highlight energy ranges where the contributions of the Si impurity and its three nearest neighbors, or that of bulk graphene, are comparatively stronger. au, arbitrary units.

Figure 1E shows, in greater detail, the phonon loss region of the spectra. The C spectrum exhibits two distinct loss peaks at 85 meV (685 cm^{-1}) and 170 meV (1371 cm^{-1}). Following (*24*), we attribute these peaks to scattering by transverse (T) or longitudinal (L), acoustic (A) or optical (O) modes in graphene, respectively (the graphene-phonon dispersion diagram is presented for reference in fig. S10). Spectral contributions of out-of-plane phonon modes are expected to be negligible, as the incident electron beam is normal to the graphene plane. Despite stemming from a position only a few atoms away, the Si spectrum shows a remarkably different phonon fine structure comprising a prominent loss peak at about 55 meV (443 cm^{-1}) and weaker structures at 125 and 150 meV (1008 and 1209 cm^{-1}). To enhance the differences between the spectra, we subtracted the C from the Si spectrum, and the resulting difference spectrum is shown in Fig. 1, E and F. This has the additional benefit of effectively subtracting the elastic scattering ZLP tail (making the reasonable assumption that the tail contribution, before any expected loss contribution, is similar between spectra) without possible errors associated with common background removal techniques, as discussed in the supplementary materials (fig. S4). Thus, the difference can be interpreted as a relative change in phonon scattering probability induced by the presence of the single Si atom impurity. Virtually identical results (detailed in the supplementary materials) were obtained from complementary measurements carried out in a different area of the sample. These experimental results lead to the remarkable conclusion that the single Si atom impurity in graphene possesses a characteristic vibrational signature localized at the atomic scale.

To gain insights into the physics associated with these results, we have calculated, within the framework of density functional theory (DFT) (*26*) and using periodic boundary conditions, the vibrational spectrum of a large 96×96 supercell of graphene (96 unit cells by 96 unit cells) containing one substitutional Si atom. The structure of the defect and computational details are presented in the supplementary materials. As discussed therein, the important features observed in the vibrational EEL spectra of graphene can be safely interpreted in terms of the phonon density of states (DOS) of the bulk. The local behavior of the DOS can be quantified by the projected phonon DOS (PPDOS), defined as $n^{\kappa}(\omega) = \sum_{\nu} |\mathbf{e}_{\nu}^{\kappa}|^2 \delta(\omega - \omega_{\nu})$, where κ denotes a specific atom, ω_{ν} and $\mathbf{e}_{\nu}$ are the phonon angular frequency and normalized polarization, and the sum is carried over all the phonon modes, ν, of the supercell. Because the momentum transfer occurs predominantly in the plane perpendicular to the electron beam trajectory in our experiments, only the components of the phonon polarization that are parallel to the graphene plane are relevant. A tentative comparison to the experimental difference spectrum is then provided by combining the PPDOS projected on the Si atom, n^{Si}; the PPDOS projected on its three C neighbors, n^{C1}; and the bulk phonon DOS per atom, n^{bulk}: $\tilde{n}(\omega) = [n^{Si}(\omega) + 3n^{C1}(\omega) - 4n^{bulk}(\omega)]/4$. This differential PPDOS reflects the experimental spectrum averaging over the scanning window, which is expected to include contributions from the impurity's neighboring C atoms. The resulting differential PPDOS is shown in Fig. 1F, after broadening to match the experimental resolution. It predicts all the main features of the experimental difference spectrum, including a single peak at ~55 meV (443 cm^{-1}), two overlapping peaks at 125 and 150 meV (1008 and 1209 cm^{-1}), and dips centered around 100 and 180 meV (807 and 1452 cm^{-1}).

The physical origin of these spectral features can be understood by considering the individual in-plane PPDOS employed to construct the differential PPDOS, $\tilde{n}$, and the PPDOS of C atoms located at increasing distances away from the Si impurity (Fig. 2A). The Si PPDOS is dominated by an intense peak at 55 meV, closely matching the low-energy experimental

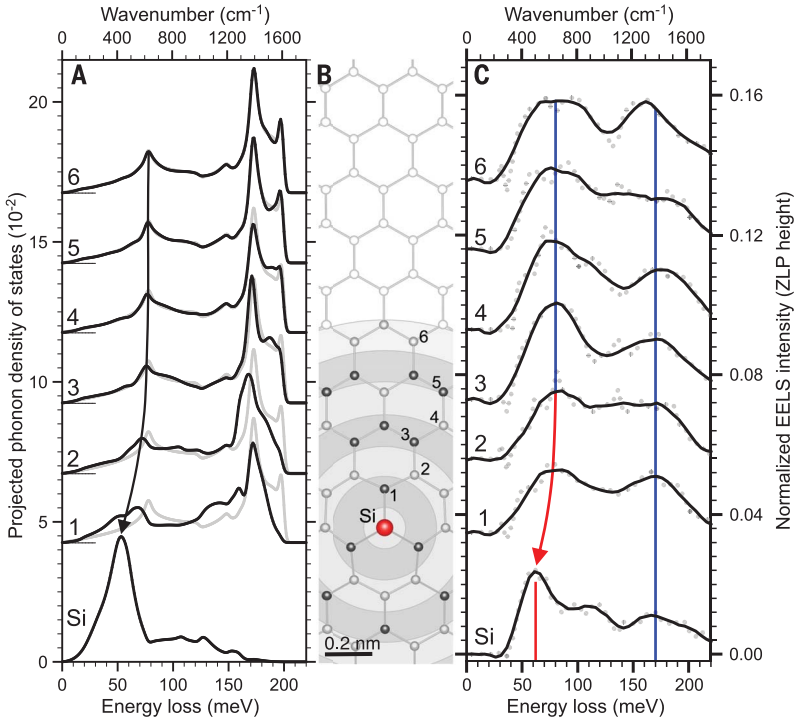

Fig. 2. Localization of the vibrational signal. (**A**) Calculated in-plane component of the phonon DOS projected on the Si and C atoms at increasing distances from the impurity. Overlaid light gray lines show the bulk graphene phonon DOS per atom, fully recovered from atom 6. The curves are vertically shifted and smeared by a 2-meV FWHM Lorentzian for clarity. (**B**) Sketch of the position of the C atoms, labeled 1 to 6, and Si impurity (red sphere). (**C**) Background-subtracted experimental spectra acquired at equivalent atomic positions. Smoothed (black lines) and raw (gray dots) data are overlaid.

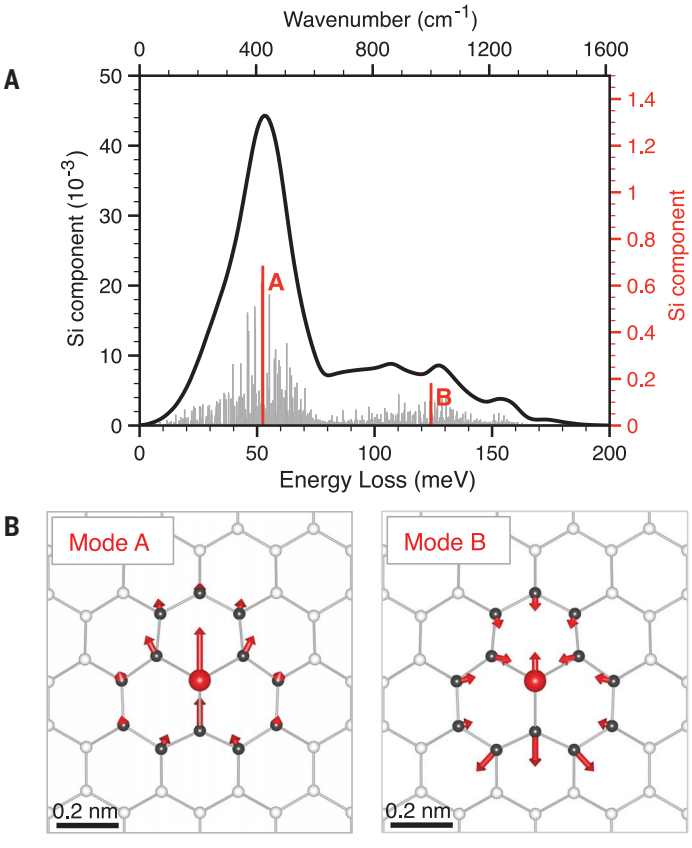

Fig. 3. Localized components of the Si vibrations. (**A**) Gray histogram shows the square of the phonon eigenmodes of the 96×96 supercell projected on the in-plane Si atom component. Black line indicates the in-plane component of the phonon DOS projected on the Si atom (same as the Si PPDOS shown in Fig. 2) obtained by broadening the gray histogram with a 2.0-meV FWHM Lorentzian. The red histogram is calculated from a 13-atom fragment centered on the impurity. Two dominant modes, denoted A and B, are observed. (**B**) Atomic model of the 13-atom fragment (the Si atom is shown in red), with relative atomic displacements for modes A and B indicated as arrows with lengths proportional to the displacement amplitudes.

feature seen in Fig. 1E. This peak is followed by a broad band with weaker structures at 105, 127, and 155 meV (847, 1024, and 1250 cm^{-1}).

The absence of intense features in the bulk graphene DOS at 55 meV implies that the corresponding modes should possess a degree of localization. By inspecting the PPDOS of neighboring C atoms in Fig. 2, it is evident that, although the first two C neighbor shells coordinating the impurity still display traces of the 55 meV peak, its contribution is weak. The PPDOS of subsequent neighbors rapidly tends toward the bulk signature, which is fully retrieved after six shells. Corresponding atomically resolved experimental spectra in Fig. 2C, from a full-spectrum image over equivalent C neighbor positions (fig. S8), exhibit an identical trend: The EELS signal reproduces the main features observed in the in-plane PPDOS.

It is instructive to consider a calculation performed on a smaller 13-atom fragment of C_{3v} symmetry centered on the impurity (fig. S9), decoupled from the supercell by artificially setting the interatomic force constants linking the fragment to the rest of the 96×96 supercell to zero. The fragment displays two modes with E symmetry at 52 and 124 meV (419 and 1000 cm^{-1}), involving large in-plane displacements of the Si atom either in phase (mode A) or out of phase (mode B) with the neighboring C atoms (Fig. 3). The resonances in the full Si@Gr system, simulated by the 96×96 supercell, can thus be interpreted as a hybridization of these local impurity modes with the vibrational continuum of the graphene bulk.

The associated atomic displacements, including those arising from the in-plane vibration of the Si atom, do not decay far from the defect; the full system presents a delocalized continuum, a concept quantified with the inverse participation ratio analysis shown in the supplementary materials. However, these delocalized phonon modes possess an enhanced component atomically localized on the impurity. The power of EELS is the technique's ability to probe this quasi-localization, thereby revealing the paradoxical nature of defect-induced resonant modes. It is also notable that the experimentally measured ~30 meV (242 cm^{-1}) full-width at half-maximum (FWHM) of the impurity peak at ~55 meV (Fig. 1F) closely matches the intrinsic theory-predicted width of the resonant mode (Fig. 3A). The experimental energy resolution is therefore not limiting, and the EEL spectra faithfully capture the fine structure of the Si@Gr system's vibrational response.

Localized and resonant modes arising from point defects have been widely discussed (*8*). The former are characterized by frequencies lying out of the continuum of the unperturbed crystal and atomic amplitudes dying off faster-than-exponentially with increasing distance from the defect (*27*). By contrast, the latter

occur at frequencies lying within the allowed bands of the host. The recognition of resonant modes was delayed by their peculiar characteristics, where the vibrational amplitude does not vanish far from the defect, extending instead over the entire crystal (*28*). Furthermore, experimental observations of these effects have, thus far, been limited to indirect fingerprints, often at the macroscopic scale. Volgmann *et al.* (*13*) used scanning probe microscope (SPM)–IETS to detect a local energy-dependent increase in phonon DOS on a Ag (100) surface, which they attributed to a substitutional Cu atom. However, the surface nature of these experiments and the lack of more direct visualization means precluded an unambiguous interpretation.

In contrast, the ability demonstrated in this work to directly measure, at the atomic scale, the localized component of the vibrational signature of a single impurity atom within a solid, and to match the observed spectral fine structure to theoretically predicted modes, realizes the potential of phonon spectroscopy in the STEM. The STEM-EELS technique, characterized by single-atom defect sensitivity combined with isotope selectivity (*17*) and the ability to operate at cryogenic temperatures (*29*), now enables potential experiments where a single functionalizing isotope is fingerprinted at the atomic scale through its vibrational signature. The approach should be applicable to three-dimensional structures, although challenges will arise from the complexity of the computational work necessary to inform these experiments. Nevertheless, this opens up a path to further applications in solid-state science, where the electron beam of the STEM can be used to assemble functional devices atom by atom (*30*) and to spectroscopically probe the resulting lattice dynamics and their coupling with other quasiparticles.

REFERENCES AND NOTES

1. W. R. Hamilton, *Philos. Trans. R. Soc.* **124**, 247–308 (1834).
2. J. W. Strutt, *The Theory of Sound* (Cambridge Univ. Press, 1887).
3. I. M. Lifšic, *Nuovo Cim.* **3**, 716–734 (1956).
4. A. S. Barker, A. J. Sievers, *Rev. Mod. Phys.* **47**, S1–S179 (1975).
5. D. J. Voneshen *et al.*, *Nat. Mater.* **12**, 1028–1032 (2013).
6. C. Brun *et al.*, *Nat. Phys.* **10**, 444–450 (2014).
7. M. Shao *et al.*, *Nat. Commun.* **5**, 3180 (2014).
8. R. F. Wallis, Ed., *Localized Excitations in Solids* (Springer, 1968).
9. O. L. Krivanek *et al.*, *Nature* **514**, 209–212 (2014).
10. T. Miyata *et al.*, *Microscopy* **63**, 377–382 (2014).
11. P. Z. El-Khoury *et al.*, *Adv. Phys. X.* **1**, 35–54 (2016).
12. H. Gawronski, M. Mehlhorn, K. Morgenstern, *Science* **319**, 930–933 (2008).
13. K. Volgmann *et al.*, *Nat. Commun.* **5**, 5089 (2014).
14. J. C. Idrobo *et al.*, *Phys. Rev. Lett.* **120**, 095901 (2018).
15. M. J. Lagos, A. Trügler, U. Hohenester, P. E. Batson, *Nature* **543**, 529–532 (2017).
16. F. S. Hage *et al.*, *Sci. Adv.* **4**, eaar7495 (2018).
17. J. A. Hachtel *et al.*, *Science* **363**, 525–528 (2019).
18. K. Suenaga, M. Koshino, *Nature* **468**, 1088–1090 (2010).
19. W. Zhou *et al.*, *Nature Nanotech.* **7**, 161–165 (2012).
20. F. S. Hage *et al.*, *ACS Nano* **12**, 1837–1848 (2018).
21. T. C. Lovejoy *et al.*, *Appl. Phys. Lett.* **100**, 154101 (2012).
22. F. S. Hage, D. M. Kepaptsoglou, Q. M. Ramasse, L. J. Allen, *Phys. Rev. Lett.* **122**, 016103 (2019).
23. C. Dwyer *et al.*, *Phys. Rev. Lett.* **117**, 256101 (2016).
24. R. Senga *et al.*, *Nature* **573**, 247–250 (2019).
25. Q. M. Ramasse *et al.*, *Nano Lett.* **13**, 4989–4995 (2013).
26. P. Giannozzi *et al.*, *J. Phys. Condens. Matter* **21**, 395502 (2009).
27. E. W. Montroll, R. B. Potts, *Phys. Rev.* **100**, 525–543 (1955).
28. R. Brout, W. Visscher, *Phys. Rev. Lett.* **9**, 54–55 (1962).
29. M. T. Hotz *et al.*, *Microsc. Microanal.* **24**, 1132–1133 (2018).
30. T. Susi *et al.*, *2D Mater.* **4**, 042004 (2017).

ACKNOWLEDGMENTS

The authors gratefully acknowledge R. Brydson, M. Bugnet, and E. Prestat for useful discussions. **Funding:** SuperSTEM is the UK National Research Facility for Advanced Electron Microscopy, supported by the Engineering and Physical Sciences Research Council (EPSRC). This work was granted access to the High-Performance Computing resources of the Institut du Développement et des Ressources en Informatique Scientifique (IDRIS) under allocation 2019-A0060910820, attributed by the Grand Equipement National de Calcul Intensif (GENCI). **Author contributions:** Q.M.R. conceived the project. F.S.H., Q.M.R., and D.M.K. designed and carried out the experiments and interpreted the data. G.R. and M.L. carried out and interpreted the theoretical calculations. All authors contributed to the preparation of the manuscript. **Competing interests:** The authors declare no competing interests. **Data and materials availability:** All data necessary for evaluating the conclusions of the paper are included in the main text and/or the supplementary materials. Data related to those presented here are available from the authors upon reasonable request.

SUPPLEMENTARY MATERIALS

science.sciencemag.org/content/367/6482/1124/suppl/DC1
Materials and Methods
Supplementary Text
Figs. S1 to S12
References (*31*–*43*)

7 November 2019; accepted 3 February 2020
10.1126/science.aba1136

Science

Single-atom vibrational spectroscopy in the scanning transmission electron microscope

F. S. Hage, G. Radtke, D. M. Kepaptsoglou, M. Lazzeri and Q. M. Ramasse

Science **367** (6482), 1124-1127.
DOI: 10.1126/science.aba1136

Seeing single silicon atom vibrations

Vibrational spectroscopy can achieve high energy resolution, but spatial resolution of unperturbed vibrations is more difficult to realize. Hage *et al.* show that a single-atom impurity in a solid (a silicon atom in graphene) can give rise to distinctive localized vibrational signatures. They used high-resolution electron energy-loss spectroscopy in a scanning transmission electron microscope to detect this signal. An experimental geometry was chosen that reduced the relative elastic scattering contribution, and repeated scanning near the silicon impurity enhanced the signal. The experimental vibration frequencies are in agreement with ab initio calculations.

Science, this issue p. 1124

Science (print ISSN 0036-8075; online ISSN 1095-9203) is published by the American Association for the Advancement of Science, 1200 New York Avenue NW, Washington, DC 20005. The title *Science* is a registered trademark of AAAS.